

Journal of
Medical Imaging

MedicalImaging.SPIEDigitalLibrary.org

**Multipurpose nonlinear optical
imaging system for *in vivo* and *ex
vivo* multimodal histology**

Martin Weinigel
Hans Georg Breunig
Aisada Uchugonova
Karsten König

Multipurpose nonlinear optical imaging system for *in vivo* and *ex vivo* multimodal histology

Martin Weinigel,^{a,*} Hans Georg Breunig,^{a,b} Aisada Uchugonova,^{a,b} and Karsten König^{a,b}

^aJenLab GmbH, Schillerstrasse 1, Jena 07745, Germany

^bSaarland University, Department of Biophotonics and Laser Technology, Campus A5.1, Saarbrücken 66123, Germany

Abstract. We report on a flexible multipurpose nonlinear microscopic imaging system based on a femtosecond excitation source and a photonic crystal fiber with multiple miniaturized time-correlated single-photon counting detectors. The system provides the simultaneous acquisition of e.g., two-photon autofluorescence, second-harmonic generation, and coherent anti-Stokes Raman scattering images. Its flexible scan head permits *ex vivo* biological imaging with subcellular resolution such as rapid biopsy examination during surgery as well as imaging on small as well as large animals. Above all, such an arrangement perfectly matches the needs for the clinical investigation of human skin *in vivo* where knowledge about the distribution of endogenous fluorophores, second-harmonic generation–active collagen as well as nonfluorescent lipids is of high interest.

© 2015 Society of Photo-Optical Instrumentation Engineers (SPIE) [DOI: 10.1117/1.JMI.2.1.016003]

Keywords: CARS; multiphoton tomography; skin imaging; second-harmonic generation; fluorescent lifetime imaging; multimodal.
Paper 14158PR received Nov. 29, 2014; accepted for publication Feb. 6, 2015; published online Mar. 4, 2015.

1 Introduction

High-resolution nonlinear deep tissue imaging^{1–3} has been realized by pixelwise focusing near-infrared (NIR) femtosecond laser pulses inside the sample and collecting fluorescence signals in the epidirection. Advantageously, the nonlinear dependence on the excitation intensity minimizes out-of-focus excitation and provides optical sectioning² with high signal to noise ratios (SNR). Additionally, the use of NIR laser radiation results in reduced out-of-focus bleaching and high penetration depths due to low scattering and low absorption of the tissue compared to one-photon excitation. The spatially resolved two-photon autofluorescence (AF) of intrinsic fluorophores, such as elastin, melanin, flavines, and NAD(P)H permits visualization of the morphological structure of the skin.⁴ Employing time-correlated single-photon counting (TCSPC)⁵ provides their characteristic fluorescence lifetimes and thus allows their distinction.¹ Marking the lifetimes in pseudocolors represents the corresponding fluorescent lifetime image (FLIM).^{1,3}

A further nonlinear optical process which can be used for deep tissue imaging is second-harmonic generation (SHG). It provides complimentary information on noncentrosymmetric protein structures of the dermal collagen network.⁶

An additional modality with optical sectioning capability is coherent anti-Stokes Raman scattering (CARS).⁷ CARS allows to detect nonfluorescent and non-SHG, but Raman-active substances. For CARS excitation, a pump (ω_{pump}), a Stokes (ω_{Stokes}) and a probe (ω_{probe}) photon are required.⁸ To simplify the CARS implementation, often the pump and probe photons are generated by a common light source ($\omega_{\text{pump}} = \omega_{\text{probe}}$). In case the frequency difference between ω_{pump} and ω_{Stokes} matches a molecular vibrational frequency, the CARS signal at $\omega_{\text{CARS}} = 2\omega_{\text{pump}} - \omega_{\text{Stokes}}$ is strongly enhanced.⁸

CARS can be applied to provide supplementary information on the distribution of lipids in human skin.^{9–12} Lipids are non-fluorescent, but rich in Raman-active CH₂ groups with a stretch vibrational transition at 2845 cm⁻¹.¹³ In human skin, they are, for instance, part of (i) the superficial skin barrier (cholesterol),¹⁴ (ii) the cellular membrane (phospholipids), and (iii) the dermis, stored inside dermal adipocytes as energy reservoirs.¹⁵ Additionally, CARS can provide information on the water distribution (OH vibration at about 3250 cm⁻¹)¹⁶ inside the skin which is of high interest, e.g., in dermatology to investigate the skin barrier function (trans epidermal water loss)¹⁷ and in cosmetic research during skin hydration measurements.¹⁸

This high wavenumber region including the vibrational transitions of lipids (CH₂), proteins (CH₃), and water (OH) can be accessed by employing commercially available photonic crystal fibers (PCF) as the source for the CARS Stokes photons.¹⁹ In fact, broadband high spectral power densities in the necessary wavelength region between 900 and 1100 nm are provided by these PCFs,¹⁹ which are inevitable for deep tissue imaging. The broadband CARS Stokes spectrum (i) can be narrowed by a bandpass filter to excite a single vibrational transition such as lipids²⁰ or (ii) can be employed to excite multiple vibrational transitions simultaneously. The latter broadband approach allows multiplex CARS (M-CARS) “spectroscopy” and “microscopy” which has been demonstrated recently by the application of supercontinuum fibers covering the detection of lipids/proteins and water.^{21–23}

The described label-free AF, SHG, and CARS modalities are perfectly in line with the needs for clinical skin imaging. During the last decade, “CE marked” AF/SHG based tomographs have been developed including systems with an additional CARS option.^{10–12,20} The certified clinical AF/SHG-CARS tomograph MPTflex CARS (JenLab, Germany) as a mobile flexible

*Address all correspondence to: Martin Weinigel, E-mail: weinigel@jenlab.de

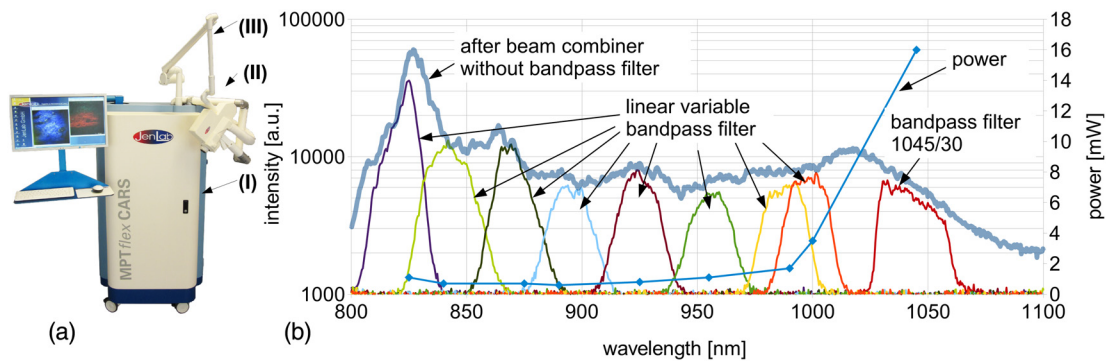


Fig. 1 (a) Flexible multimodal tomograph MPTflex CARS and (b) spectral characteristics of the employed photonic crystal fiber.

nonlinear imaging system not only simplifies *in vivo* AF/SHG imaging of human skin^{9,24–26} but is also a multipurpose system which can be used for small animal research, *in vivo* stem cell tracking²⁷ and *ex vivo* biopsy imaging. Free-space-beam delivery inside an articulated optical mirror arm is provided by active beam position control. This allows a high degree of freedom for the positioning of the scan head, inevitable for a variety of medical applications [Fig. 1(a)].^{26,28,29}

The scan head of the tomograph MPTflex CARS typically contains a dual-channel detector for simultaneous detection of AF and SHG or AF/SHG and CARS signals, respectively. Its laser scanning arrangement allows to acquire AF/SHG and CARS images with a field-of-view (FOV) of $350 \times 350 \mu\text{m}^2$ and $200 \times 200 \mu\text{m}^2$, up to a depth of 200 and 150 μm , respectively. However, due to the limited number of detectors, a separation of simultaneously generated AF and SHG signals during CARS imaging was not possible. Thus, e.g., skin aging studies based on the SHG-to-AF aging index of dermis (SAAID)³⁰ were limited to non-CARS tomographs.

In this article, we report on a very compact multichannel-(FLIM)-detector for the clinical tomograph MPTflex CARS, which satisfies the need for simultaneous detection of multiple signals. This paper is divided into three sections: (i) the system characterization, (ii) *ex vivo* imaging of murine tissue samples, and (iii) the application on human skin *in vivo*.

2 Materials and Methods

2.1 Experimental Setup

A detailed description of the imaging system MPTflex CARS [Fig. 1(a)] was published recently.¹⁰ Briefly, the system consists of a mobile optoelectronic housing (I) and a freely movable and adjustable scan head (II) connected to the housing (I) by a flexible articulated mirror arm (III). For CARS contrast, the pulses (centered at 800 nm) from an 80 MHz Ti:sapphire, 100 fs oscillator (MaiTai XF-1, Spectra Physics, USA) are divided into two parts. One part, which passes a motorized delay line, is used as both CARS pump and probe. The remaining part is coupled into a PCF (FemtoWHITE CARS, NKT Photonics, Denmark) for spectral broadening.

The spectral characteristics of the PCF are presented in Fig. 1(b). The bold blue curve represents the full spectrum of the PCF behind the dichroic beam combiner SP850 with a total power of about 65 mW. Note that the applied spectrometer (BTC112E TE, B&W Tek) is not intensity calibrated for this

measurement. The spectral density of the fiber is determined separately by placing a linear variable bandpass filter (LVNIRBP, Delta Optical Thin Film A/S, Denmark) behind the dichroic beam combiner SP850 and measuring its transmitted optical power at the individual transmitted spectral bands. The corresponding integrated optical power of these spectral bands is also shown in Fig. 1(b). Spectral power densities at 1045 nm are about (16 mW/30 nm) \approx 0.5 mW/nm and at 825 nm, spectral power densities are about 0.07 mW/nm.

The bandpass filtered output [in general: centered at 1045 nm, 30-nm full width at half maximum (FWHM)] is used as the CARS Stokes laser and allows one to generate CARS contrast at 2845 cm^{-1} to probe the Raman resonances of lipids and proteins. Collinearly recombined by a dichroic beam combiner, the two beams are coupled into the articulated mirror arm in a free-space setup. On axis beam delivery through the articulated mirror arm is guaranteed by active beam stabilization, which compensates for any temperature drift of the system's optomechanical structure and the mechanical tolerances of the articulated mirror arm. This beam stabilization is an essential element of the presented imaging system. Due to the relative long beam path ($\approx 3.5 \text{ m}$), even minor mechanical tolerances can translate to a significant position error at the back aperture of the focusing optics. The consequence would be a noncentered illumination of the FOV and thus a strong degradation of image quality.

The deviations of the CARS pump and Stokes excitation beams from the target position are successively detected by a position-sensitive detector located at a conjugated position of the focusing optics inside the scan head [see Fig. 2(a)]. The rear surface reflection of the dichroic beam splitter is used as a test beam. The feedback signals of the position-sensitive detector are sent to the computer which controls two motorized kinematic mirror mounts located in front of the articulated mirror arm.

This active beam stabilization and an additional motorized delay line guarantee the necessary spatial and temporal overlap, respectively, of the CARS pump and CARS Stokes pulses inside the focal volume of the 40×1.3 numerical aperture focusing optics. The multitude of generated signals which are detectable by the system include AF, SHG_{pump} , $\text{SHG}_{\text{Stokes}}$, sum frequency generation ($\text{SFG}_{\text{pump}+\text{Stokes}}$) of the CARS pump and CARS Stokes photons and the CARS signals.

For a simultaneous detection and separation of AF/FLIM, SHG and CARS signals, a compact four-channel detection module has been specially developed by us for the scan head of

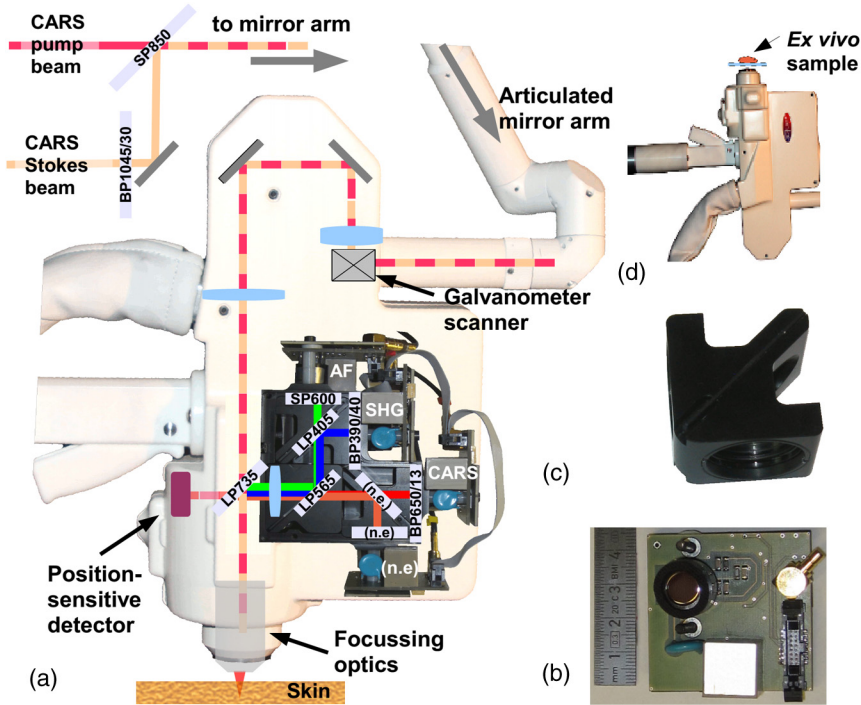


Fig. 2 (a) Schematic beam path inside the scan head with four-detector arrangement; (b) miniaturized detector electronics; (c) filter cube; (d) inverted scan head position for *ex vivo* imaging. AF: autofluorescence; SHG: second-harmonic generation; CARS: coherent anti-Stokes Raman scattering; n.e., not employed.

the tomograph MPTflex CARS [see Fig. 2(a)]. The miniaturized printed circuit board for a single detector is presented in Fig. 2(b). The quantum efficiencies of the photomultiplier tube (PMT) sensor elements are $>30\%$ for the AF spectral range (PMT R9880U-210) and $>15\%$ for the CARS detection channel (PMT R9880-20).

Compared to previous detector designs, several advantages are provided by the new detection module: (i) fast temporal responses of all four detectors and the corresponding electronics, (ii) lightweight mechanical design that seals off the detector active areas against ambient light which is inevitable for the clinical environment, and (iii) changeable filter cubes [see Fig. 2(c)].

Short pass filters are used to separate signal light from residual back-scattered excitation light. A longpass dichroic mirror LP565 separates the AF/SHG- and CARS signals, respectively. The CARS detection channel (3) is spectrally further narrowed to 13 nm (FWHM) centered at 650 nm. The AF/SHG beam path was split by a longpass dichroic mirror LP405 nm into an AF channel (1) equipped with a shortpass SP600 nm filter to block the residual CARS signals. A 40-nm bandpass filter centered at 390 nm in front of the SHG channel (2) blocks residual AF signals. [Channel (4) was not employed (n.e.) in this setup and the experiment, but offers the possibility to detect further signals.]

The simultaneous readout of the detectors was accomplished by single-photon counting (SPC) hardware (JenLab, Germany) generating images of 512×512 pixels at a mean dwell time of $26 \mu\text{s}/\text{pixel}$. [This corresponds to about 6.5 s/frame. Higher frame rates are possible, e.g., for an overview image of the region-of-interest (ROI), however, with a lower SNR.] Lifetime measurements can be accomplished simultaneously to SPC by TCSPC hardware SPC 150 (Becker&Hickl, Germany) with

a standard resolution of 128×128 pixels (alternative pixel resolution settings are possible). In the following experiments, TCSPC data are presented only for channel (1), but in principle, all four channels can be readout by the same TCSPC hardware using the integrated TCSPC router electronics HRT-41 (Becker&Hickl, Germany).

2.2 Spatial Resolution Measurement

Axial and lateral resolution was measured for AF and CARS modalities in epidirection without averaging. As a figure of merit for the lateral resolution of the imaging system, spin-coated subresolution microspheres were imaged and the FWHM of their point spread function was measured. For AF and CARS imaging, $0.20 \mu\text{m}$ yellow/green fluorescent microspheres (Fluoresbrite™ Plain YG Microspheres, Polyscience, USA) and $0.21 \mu\text{m}$ polystyrene microspheres (PS02N, Bangs Laboratories, USA) were recorded, respectively, with pixel dwell times of $11 \mu\text{s}/\text{pixel}$ (512×512 pixels). A Gaussian fit was applied to the line intensity profile through the center of imaged sub-resolution microspheres. To determine the axial resolution, the derivative of the edge response during the transition from cover glass to fluorescein solution (AF) and from cover glass to glycerol (CARS) has been used as a figure of merit,³¹ respectively. A stack of $0.1\text{-}\mu\text{m}$ separated images was recorded and a Gaussian fit was applied to the first derivative of the mean intensity distribution along the z direction. The power for AF imaging at 800 nm was set to 0.2 mW and for CARS imaging, 5 mW and 3 mW for the CARS pump and CARS Stokes laser, respectively. To increase the amount of backscattered light (similar to human skin), a piece of white label paper was placed in the optical axis directly behind the focal volume.

2.3 Validation of the FLIM System

FLIM capability has been verified (i) by determining the temporal resolution of the complete imaging system and (ii) measuring the lifetime of fluorescein solution as a reference. As a figure of merit for the temporal resolution of the complete imaging system, the FWHM of the instrument response function (IRF) has been measured. The IRF has been determined by detecting SHG from the nonlinear interaction of the 800-nm excitation radiation (CARS Stokes laser was blocked) with urea crystals and recording its apparent time duration by the TCSPC software package (SPCImage, Becker & Hickl, Germany).

Additionally, the lifetime of the fluorescein solution (Fluorescein SE Thilo 1.7 mg/ml Fluorescein-Natrium; Alcon Pharma, Germany) as a standard test sample was acquired. To suppress self-quenching effects, the initial concentration of the fluorescein solution (0.17%) has been diluted to about 0.002%. For this measurement, the effective IRF was automatically determined by the TCSPC software package.

2.4 Determination of Chemical Contrast

The chemical contrast of lipids was measured by imaging a three-dimensional (3-D) structured chess pattern test target (70- μm grating constant) made of borosilicate glass whose cavities were filled with immersion oil (type 518 F; Zeiss, Germany). The lateral intensity profile through the center of the position of an oil-filled cavity and the position of the sole glass next to it was determined. The CARS-independent background, composed of brightness bias, detector noise, and AF/laser leakage, was compensated by acquiring an image without the temporal overlap of CARS pump and CARS Stokes pulses (temporal detuning of >5 ps). The ratio of resonant (R) to nonresonant background (NRB) was determined by subtracting the mean intensity value (I_B) of this background from the acquired lateral intensity profile $I[R/\text{NRB} = (I_{\text{MAX}} - I_B)/(I_{\text{MIN}} - I_B)]$. Similar to the above described resolution measurements, the amount of backscattered light was increased by a piece of white label paper placed directly behind the focal volume.

2.5 Ex Vivo Imaging

To demonstrate *ex vivo* imaging, the inverted scan head position was set up as shown in Fig. 2(d). Animal studies have been conducted in accordance with ethical standards. Fresh murine tissue samples (extracted 5 h postmortem) of brain, abdominal fat, intestine, liver, spinal cord, and muscle from a hairy mouse were placed on an N-BK7 coverslip connected by double sided tape with the system associated adapter ring. The XY and Z positioning of the tissue relative to the focus position was realized by an integrated motorized stage with maximum vertical and axial travel distances of $5 \times 5 \text{ mm}^2$ and 5 mm and a step size of 12.7 μm and 1.25 μm , respectively.

All images were acquired with total optical powers ($P_{\text{pump}} + P_{\text{Stokes}}$) in the range of 10 to 40 mW at the sample position at imaging depths of 5 to 30 μm and without averaging. For better print-visualization of individual images, their contrast has been enhanced using ImageJ software.³²

2.6 In Vivo Human Skin Imaging

For human skin imaging, immersion oil (type 518 F; Zeiss, Germany), N-BK7 coverslips, and water were placed between focusing optics and skin. To comply with laser safety

requirements of the certified body, the total output power of both beams ($P_{\text{pump}} + P_{\text{Stokes}}$) was limited to 50 mW at the skin. Imaging was performed on healthy human skin (male forearm and nasal wing) in a skin depth of 70 and 5 μm , respectively.

2.7 Multiplex CARS

In order to realize M-CARS, the Stokes-bandpass filter [see Fig. 2(a)] was replaced by a longpass LP785. “M-CARS spectroscopy” (forward detected; pump-laser centered at 782 nm) was realized to demonstrate the chemical selectivity. Multiplex CARS is accomplished by spectral focusing.³³ The necessary chirp is passively achieved by the dispersive elements inside the optical beam path. CARS spectra of water, glycerol and dimethylsulfoxide (DMSO) were acquired using a fiber-coupled spectrometer (BTC112E TE, B&W Tek, USA; 60-s integration time) with a collimator lens attached to the collection side of the fiber. To compensate spectral power density variations of the supercontinuum, the acquired spectra of water, glycerol and DMSO were normalized against the nonresonant signal generated inside an N-BK7 slide in a similar way as described by Kano.³⁴

For “M-CARS imaging” of test samples containing water and oil, the accessibility of the OH region was realized by tuning the wavelength of the CARS pump laser to 788 nm. For separation of lipid-CARS and water-CARS signals, a dichroic long-pass beam splitter LP640 was combined with a 13 nm bandpass filter with a transmission maximum centered at a wavelength of 640 nm [lipid channel (3)] and a 15 nm bandpass filter with a transmission center wavelength at 625 nm [water channel (4)]. As a proof of principle demonstration, an interface of water and petroleum jelly (Vaseline® original, Unilever, Germany) was imaged. Considering the chirp of the Stokes pulses, images were acquired at different temporal delay positions (+0.25 ps = maximum signal in lipid channel; -0.25 ps = maximum signal in water channel; ± 0 ps = signal in both channels).

Finally, the “M-CARS imaging” capability was tested on fresh murine abdominal fat tissue.

3 Results

3.1 Spatial Resolution Measurement

The mean FWHM for AF- and CARS-lateral intensity profiles was determined to be $(0.39 \pm 0.02) \mu\text{m}$ (emission maximum at about: 486 nm) and $(0.28 \pm 0.03) \mu\text{m}$ (emission at: 651 nm), respectively. Typical intensity profiles are illustrated in Figs. 3(a) and 3(c). The FWHM of the derivative of the AF and CARS intensity edge response was determined to be $(1.85 \pm 0.15) \mu\text{m}$ (emission maximum at about: 520 nm) and $(1.53 \pm 0.12) \mu\text{m}$, respectively. Typical responses are visible in Figs. 3(b) and 3(d).

3.2 Validation of the FLIM System

A typical IRF is illustrated in Fig. 3(e) with an FWHM of 200 ps. The fluorescence decay curve of fluorescein [Fig. 3(f)] shows a monoexponential decay [fitting settings: monoexponential best-fit curve (dashed); threefold binning]. The decay time distribution histogram of fluorescein with a single maximum is presented in Fig. 3(g).

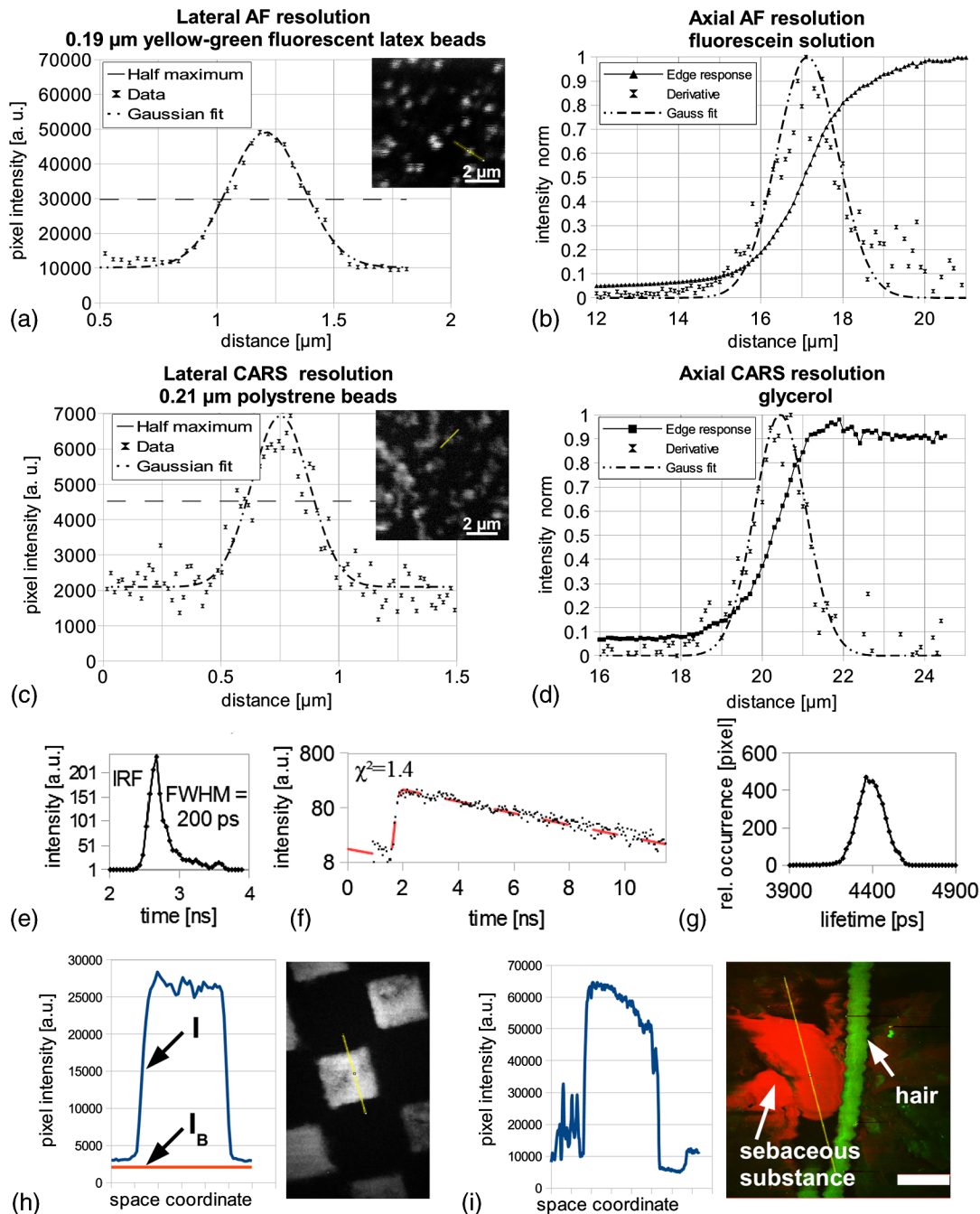


Fig. 3 (a) Lateral two-photon autofluorescence (AF) intensity profile of a subresolution fluorescent microsphere; (c) lateral coherent anti-Stokes Raman scattering (CARS) intensity profile of a polystyrene microsphere; (b) and (d) intensity edge responses and corresponding derivatives of a glass/fluorescein and glass/glycerol interface, respectively; (e) temporal instrument response function (IRF) of the imaging system; (f) typical decay function and (g) lifetime distribution histogram of fluorescein solution; (h) characterization of resonant to nonresonant background ratio at an oil/glass interface and (i) at the exit of sebaceous gland (human skin *in vivo* from the nasal wing, scale bar: 20 μm).

3.3 Determination of Chemical Contrast

The CARS image of the 3-D structured test target whose cavities were filled with immersion oil is shown in Fig. 3(h) with the lateral CARS intensity profile (I , blue) through the center of an oil-filled cavity and the mean background signal (I_B , red). Subtraction of I_B (non-CARS background) from I reveals a ratio R/NRB of about 27:1.

3.4 Ex Vivo Imaging

Multimodal images of fresh murine brain, abdominal fat tissue, intestine, liver, myelin sheaths, and abdominal muscle are shown in Fig. 4. The optical section of the abdominal fat tissue indicates a strong CARS contrast due to high CH_2 concentrations inside the monovacuolar adipocytes. The adipocytes are connected to each other by reticular collagen fibers (SHG)

and the fluorescence contrast is visible from the periphery of the cells. Interestingly, the lifetime image accentuates a further capillary-like structure (arrowhead), which is difficult to recognize in the AF or SHG channel. High lipid concentrations are also present inside liver tissue as intracellular lipid vacuoles/droplets, inside the spinal cord as myelin sheaths and in between muscle tissue as adipocytes, respectively. Images of muscle tissue additionally show highly periodic SHG contrast due to myofilaments.

3.5 *In Vivo* Human Skin Imaging

Multichannel AF/FLIM-SHG-CARS functionality on healthy human skin *in vivo* at a depth of 70 μm (dermal papillae) is demonstrated in Fig. 5. The AF channel represents a circular arrangement of basal cells with elastin fibers in the center. The corresponding lifetime image reveals the heterogeneity of lifetimes (pseudocolors). The SHG channel visualizes the corresponding interweaved collagen fibers due to the nonlinear light–collagen interaction. The CARS channel shows sharply separated cellular details but also roundish structures of dermal papillae are noticeable.

Figure 3(i) shows an optical section of human skin from the nasal wing. The CARS signal (red) points out high lipid concentrations of sebum on the surface of the skin. The AF signal (green) illustrates a hair and corneocytes.

3.6 Multiplex CARS

The glycerol CARS spectrum [Fig. 6(b), black] reveals two significant peaks, the CH_2 peak at 2845 cm^{-1} and the OH peak at 3250 cm^{-1} . The latter is caused by the OH-stretching vibration of the glycerol molecule and the high-water content of glycerol (about 14% in accordance with the pharmacopoeia). The DMSO spectrum (red) was recorded to characterize the spectral resolution of the CARS system. The Raman band at 2916 cm^{-1} can be clearly distinguished from the band at 3000 cm^{-1} . The CARS spectrum of water (blue) has a maximum at 3250 cm^{-1} . Notice that the intensities were normalized and the OH intensities correspond to one-fourth of the CH_2 intensities.

M-CARS imaging at the interface of water and petroleum jelly [Fig. 6(a)] at different temporal delay positions reveals a significant contrast reversal from the CH_2 to the OH channel. At zero delay, both channels simultaneously detect vibrational

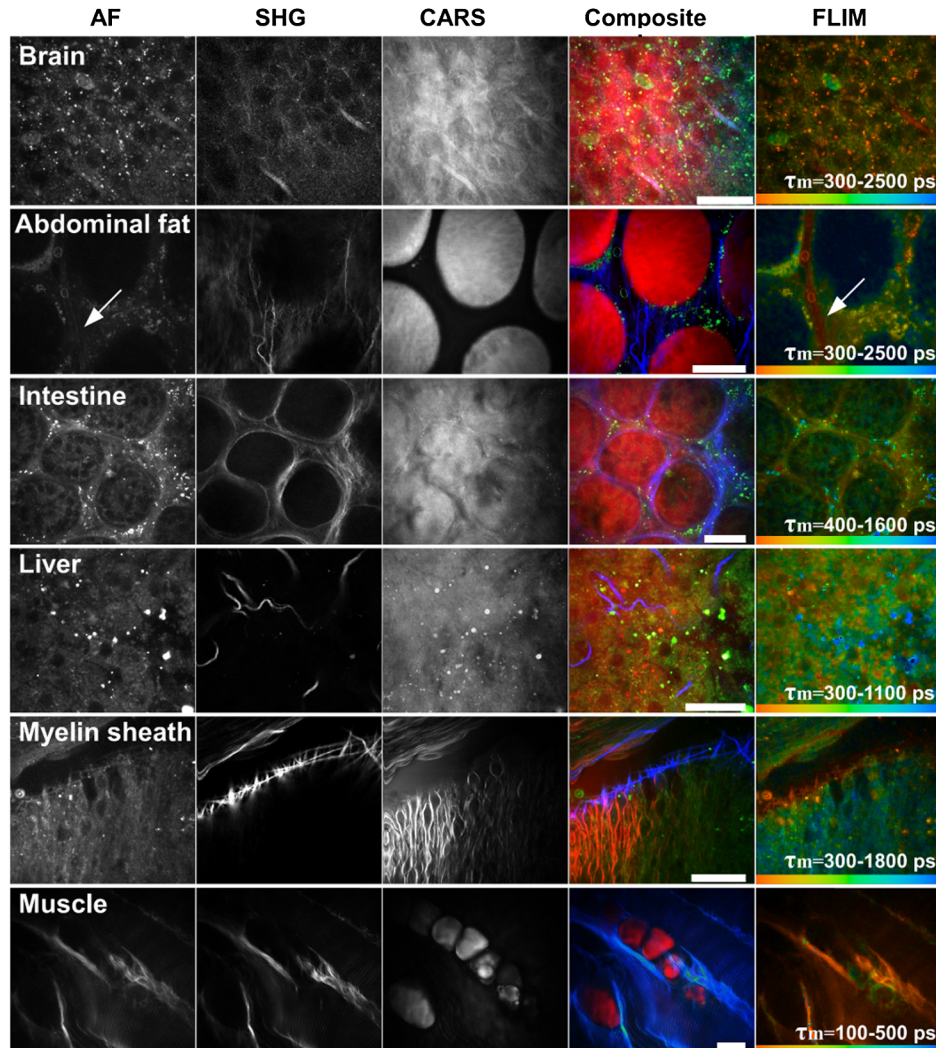


Fig. 4 *Ex vivo* examination of various murine tissues; AF: autofluorescence; SHG: second-harmonic generation; CARS: coherent anti-Stokes Raman scattering; FLIM: fluorescence lifetime imaging (τ_m = mean lifetime); CARS pump laser: 800 nm; CARS Stokes laser: 1035 nm. Scale bar: 30 μm .

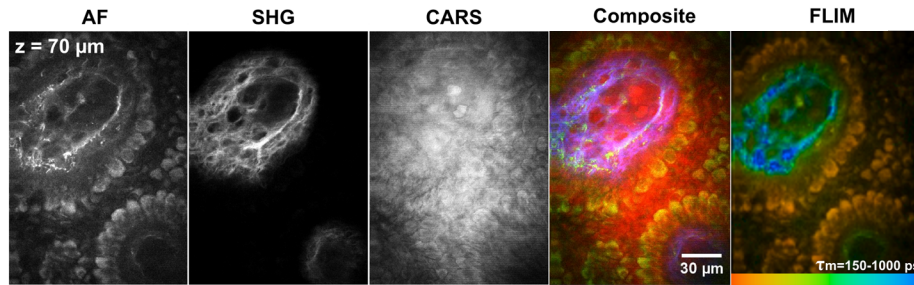


Fig. 5 Multichannel imaging of human skin *in vivo* (forearm, dermal papillae at 70 μm imaging depth); AF: autofluorescence; SHG: second-harmonic generation; CARS: coherent anti-Stokes Raman scattering; FLIM: fluorescence lifetime imaging (τ_m = mean lifetime).

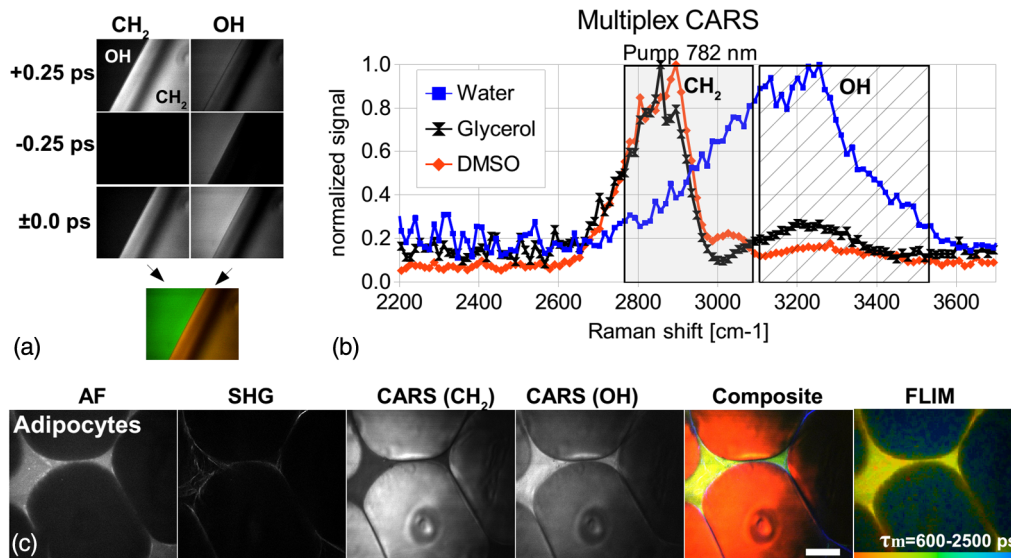


Fig. 6 Broadband multiplex coherent anti-Stokes Raman scattering (M-CARS) imaging; (a) M-CARS capability at petroleum jelly/water interface; (b) CARS spectrum of water, glycerol and dimethylsulfoxide (DMSO); (c) autofluorescence (AF), second-harmonic generation (SHG), fluorescence lifetime images (FLIM) and multiplex (M)-CARS images of abdominal fat tissue. Scale bar: 30 μm .

related signals with sufficient contrast between water and petroleum jelly.

Furthermore, the capability for M-CARS imaging was tested on murine abdominal fat tissue seen in Fig. 6(c). Next to the high contrast of the AF and SHG modalities, a high contrast can be also visualized between intracellular lipids and extracellular water. The composite image in Fig. 6(c) shows the signals pseudocolored (AF: green, SHG: blue, CH_2 -CARS: red, and OH-CARS: yellow). The FLIM data disclose additional, lifetime-dependent contrast, with granular structures in between the intracellular lipid matrix.

4 Discussion

4.1 Spatial Resolution Measurement

Nonflexible multiphoton tomographs based on stable breadboard designs have a typical resolution of about 300 nm.¹ It should be noticed that the gained flexibility of the MPTflex CARS due to the optical articulated mirror arm results in a 3.5-m long optical beam path. This influences the spatial resolution due to a possible jitter between the two beams and the optical axis as well as between the two beams. Interestingly, the above described resolution measurements clearly reveal

an excellent subcellular resolution of <400 nm which is close to the one of a stable breadboard design but with the advantage of significantly more flexibility and thus accessibility for *in vivo* imaging.

4.2 Validation of the FLIM System

Essential for the acquisition of lifetime data (FLIM) is a fast response of the detector and the electronics of the imaging system. The novel multichannel detector reveals a representative IRF with an FWHM of about 200 ps, which is of the order of previous multiphoton imaging systems.³⁵ Furthermore, the lifetime distribution histogram exhibits a single maximum at 4.4 ns, which coincides with literature values ranging from 4.1 ns to 4.5 ns.^{36,37}

4.3 Determination of Chemical Contrast

In the applied femtosecond CARS system, the spectral resolution is set by the spectral width of the CARS pump laser, where a pulse width of 100 fs corresponds to a spectral width of about 150 cm^{-1} , which is generally much broader than the line width of many Raman resonances.³⁸ The chemical contrast for the

excitation of narrow Raman lines is reduced due to noninvolved spectral parts of the CARS pump laser. In this manner, the generated NRB limits the chemical contrast, which makes it difficult for the system to be applied for the fingerprint region.³⁹ In the high wavenumber region, the situation is different. The broad Raman line width at a resonance of 2845 cm^{-1} CH_2 (lipids) and 2950 cm^{-1} CH_3 (proteins)⁴⁰ roughly fits to the spectral width of the femtosecond pulses and thus supports the sensitivity and the ratio R/NRB . In fact, Chen et al. demonstrated that the vibrational contrast at 2845 cm^{-1} for picosecond as well as femtosecond CARS systems are comparable.⁴¹

These findings are also confirmed by the R/NRB measurement at the 3-D structured test target filled with oil ($R/\text{NRB} = 27:1$) but also *ex vivo* on fresh murine myelin sheaths (see Fig. 4) with a vibrational contrast of $>7:1$, which are similar to contrast ratios observed by other groups.⁴¹ For most parts of the epidermis and upper dermis of human skin, the R/NRB is significantly lower due to lower concentrations of lipids. R/NRB ratios of about 3:1 (data not shown here) have been determined by our group, however, some ROIs like the exit of sebaceous glands on the skin surface disclose higher lipid concentrations (sebum) and thus reveal higher R/NRB ratios in a range between 10:1 and 20:1 [see Fig. 3(i)].

4.4 Ex Vivo Imaging

The application of the described multichannel detector uncovers valuable complementary information, such as seen in the murine tissue images of Fig. 4. To exemplify, a capillary like structure (arrowhead in Fig. 4), which is very challenging to be recognized in the AF or SHG channel, is highlighted inside the lifetime image. There are even blood cells visible inside this capillary.

In Fig. 4, the muscle tissue shows similar information inside the SHG and the AF image. This is most likely due to nonlinear interaction at the muscle fibrils producing a $\text{SHG}_{\text{Stokes}}$ signal at a wavelength of 517 nm (and possibly also due to the $\text{SFG}_{\text{Pump}+\text{Stokes}}$ signal at a wavelength of 451 nm). For effective suppression of the $\text{SHG}_{\text{Stokes}}$ and $\text{SFG}_{\text{Pump}+\text{Stokes}}$ signals inside the AF image, spectral notch filters can be applied. Furthermore, the application of TCSPC hardware allows a temporal separation between the instantaneous SHG and SFG signals (fast components) and the decayed fluorescence lifetime component by the application of time gating.⁴²

Even though the images of Fig. 4 represent *ex vivo* data, such data sets can also be generated *in vivo*. This has already been demonstrated over a time period of several hours on living mice with the AF and SHG imaging capability of the MPTflex (JenLab, Germany).²⁷

4.5 In Vivo Human Skin Imaging

Subcellular details are visible inside the multimodal *in vivo* section of Fig. 5. In addition to the morphology accessible in the AF and SHG images, the lifetime image reveals a heterogeneity of lifetimes which is the result of different endogenous fluorophores and their microenvironments inside the skin (settings: double-exponential best-fit, threefold binning). The basal cells can be clearly distinguished (orange color coded; high content of melanin⁴) from the elastin (blue–green color coded; longer lifetimes).¹ The CARS image provides additional morphological information.

There is no significant AF crosstalk visible in the SHG image. However, for deeper skin regions, a weak $\text{SHG}_{\text{Stokes}}$ and $\text{SFG}_{\text{Pump}+\text{Stokes}}$ signal from the nonlinear interaction at collagen molecules of the dermis cannot be excluded. In general, this can be easily eliminated by the same methods already discussed above including the application of spectral notch filters or by applying time gating.

4.6 Multiplex CARS

The proof of concept experiment in Fig. 6 shows that broadband multiplex CARS imaging with a simultaneous detection and separation of lipids/proteins and water has been realized. With the filters and beamsplitters used in this study, the spectral separation between the CH_2 and OH vibration occurred at the position of 3100 cm^{-1} . The CH_2 detection channel (gray shaded background) is separated from the OH detection channel (hatched background) by a few wavenumbers only [see Fig. 6(b)]. This results in a possible detection of the OH side wing by the CH_2 channel. Even though the normalized OH intensities correspond to one-fourth of the CH_2 intensities, this crosstalk is not negligible at 3100 cm^{-1} . In future, this crosstalk can be reduced by an appropriate filter assembly with a spectral separation close to 3000 cm^{-1} .

The CARS spectrum of water has a maximum at around 3250 cm^{-1} which is similar to the CARS spectrum published by Slepko et al.²³ To determine the spectral resolution of the system, a CARS spectrum of DMSO was recorded. It shows two clearly distinguished peaks at 2916 cm^{-1} and at about 3000 cm^{-1} . However, the appearing spectral resolution is higher than the one expected from the CARS pump pulse spectral width (150 cm^{-1}) which is due to the present chirp of the CARS pump and/or CARS Stokes pulse(s). In future, the chemical contrast of the presented M-CARS imaging approach might be enhanced by system adaption such as further spectral focusing which could be advantageous for separating lipid and protein signals.

4.7 Considerations on Data Handling

The signals of a multitude of modalities can be recorded simultaneously by the described multichannel detector. It is obvious that the amount of generated data increases with the number of applied channels. One SPC image (bit depth: 16 bit) of 512×512 pixels generates 0.5 MB of data. Acquiring a typical stack of 20 images (z -step $10\text{ }\mu\text{m}$) and applying all four channels creates about 40 MB of data per image stack. For an estimated minimum of three stacks, the amount of data increases to 120 MB per patient or lesion. Additional data accumulates when adding the lifetime modality. As an example, Fig. 7(a) represents pseudocolored FLIM data of human dermis. The number of photons per pixel (SPC) is shown in Figs. 7(c) and 7(d) of a single elastin fiber. Pixels with photon numbers >800 are red and others are green colored, respectively. Altogether, the framed pixels (onfold binning) contain 6300 photons with their arrival time represented as a temporal decay curve in Fig. 7(b) (double exponential fit). The additional lifetime information is of high value for functional imaging of the tissue, which however, requires at least 8 MB (related to 128×128 pixels) of disk space for only one lifetime image. (It is possible to acquire the lifetime data of four channels simultaneously, with a higher resolution of 512×512 pixels which, however, would exceed this discussion.) Completing

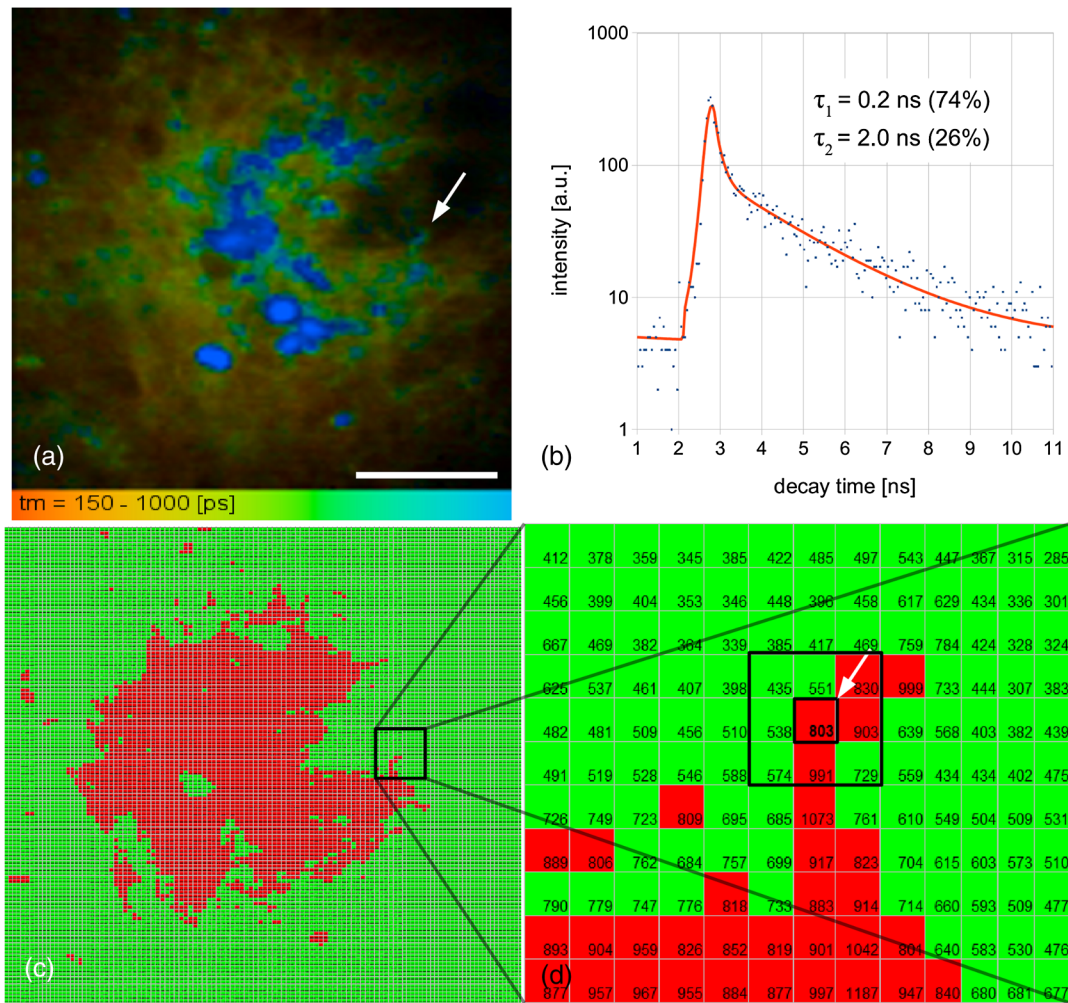


Fig. 7 (a) Fluorescence lifetime image of upper dermis; (b) decay curve of the marked pixel (arrowhead; elastin fiber) in (a); (c) single photon counting image (pixel color: ≤ 800 = green; > 800 = red); and (d) magnified section of the framed part in (c). Scale bar: $40 \mu\text{m}$.

this discussion, the data for one typical examination will generate data exceeding 0.5 GB.

The analysis of the acquired data in multiphoton imaging is still handled manually which limits the patient throughput. In future, automated image analysis will be required. Especially, the quantification of photon numbers for skin aging measurements³⁰ and qualitative analysis such as extraction of diagnostic relevant data for skin cancer detection^{28,29} require sophisticated computer-aided diagnosis (CAD),⁴³ which in the future should be combined with clinical multiphoton tomographs.

5 Conclusion

A multipurpose, multimodal, and mobile imaging system with superior optical sectioning capability has been presented. A multitude of information including AF/FLIM, SHG, and CARS can be obtained in a single scan. Several applications could benefit from this multichannel detector such as *ex vivo* imaging of excised tumor tissue⁴⁴ or SAAID-based skin aging measurements³⁰ of human skin. Visualization of lipid/protein and water contrast enables further applications in dermatology to investigate skin barrier problems¹⁷ or in cosmetic research for skin hydration measurements,¹⁸ such as depth profiles of skin lipids and water. Optical sections of human skin can be realized

completely painlessly with high-resolution images acquired in a few seconds. Additionally, the integrated XYZ motorized stage allows easy tissue positioning for *ex vivo* (inverted imaging system) as well as *in vivo* human skin imaging in a $5 \times 5 \text{ mm}^2$ ROI and an axial travel distance (Z) of 5 mm for easy and fast localization of the tissue/skin surface.

A future step will be the integration of a sophisticated CAD to handle the significant amount of acquired data and thus to increase patient throughput.

Acknowledgments

The work was supported by the German Federal Ministry of Education and Research (BMBF) under the national projects Chemoprävent 13N10507 and Biofeedback 13N12594.

References

1. K. König and I. Riemann, "High-resolution multiphoton tomography of human skin with subcellular spatial resolution and picosecond time resolution," *J. Biomed. Opt.* **8**(3), 432–439 (2003).
2. W. Denk, J. H. Strickler, and W. W. Webb, "Two-photon laser scanning fluorescence microscopy," *Science* **248**(4951), 73–76 (1990).
3. B. R. Masters, P. T. So, and E. Gratton, "Multiphoton excitation microscopy of *in vivo* human skin. Functional and morphological optical biopsy

- based on three-dimensional imaging, lifetime measurements and fluorescence spectroscopy," *Ann. New York Acad. Sci.* **838**, 58–67 (1998).
4. K. König, "Clinical multiphoton tomography," *J. Biophotonics* **1**(1), 13–23 (2008).
 5. W. Becker, *Advanced Time-Correlated Single-Photon Counting Techniques*, pp. 20–24, Springer, Berlin, Heidelberg, New York (2005).
 6. P. J. Campagnola et al., "Three-dimensional high-resolution second-harmonic generation imaging of endogenous structural proteins in biological tissues," *Biophys. J.* **82**(1 Pt 1), 493–508 (2002).
 7. A. Zumbusch, G. Holtom, and S. Xie, "Three-dimensional vibrational imaging by coherent anti-stokes raman scattering," *Phys. Rev. Lett.* **82**, 4142–4145 (1999).
 8. N. Bloembergen, "A quarter century of stimulated Raman scattering," *Pure Appl. Chem.* **59**, 1229–1236 (1987).
 9. K. König, "Hybrid multiphoton multimodal tomography of *in vivo* human skin," *IntraVital* **1**(1), 11–26 (2012).
 10. M. Weinigel et al., "In vivo histology: optical biopsies with chemical contrast using clinical multiphoton/CARS tomography," *Laser Phys. Lett.* **11**, 055601 (2014).
 11. H. G. Breunig et al., "Clinical coherent anti-Stokes Raman scattering and multiphoton tomography of human skin with a femtosecond laser and photonic crystal fiber," *Laser Phys. Lett.* **10**(2), 025604 (2013).
 12. H. G. Breunig et al., "Combined *in vivo* multiphoton and CARS imaging of healthy and disease-affected human skin," *Microsc. Res. Tech.* **75**(4), 492–498 (2012).
 13. X. Nan, J.-X. Cheng, and X. S. Xie, "Vibrational imaging of lipid droplets in live fibroblast cells with coherent anti-Stokes Raman scattering microscopy," *J. Lipid Res.* **44**(11), 2202–2208 (2003).
 14. P. W. Wertz, "Lipids and barrier function of the skin," *Acta dermatovenerologica. Supplementum* **208**, 7–11 (2000).
 15. G. Thews, E. Mutschler, and P. Vaupel, *Anatomie Physiologie Pathophysiologie des Menschen*, 5th ed., pp. 15–6 and 751–761, Wiss. Verl.- Ges., Stuttgart (1999).
 16. W. Min et al., "Coherent nonlinear optical imaging: beyond fluorescence microscopy," *Annu. Rev. Phys. Chem.* **62**, 507–530 (2011).
 17. E. Proksch, J. M. Brandner, and J. M. Jensen, "The skin: an indispensable barrier," *Exp. Dermatol.* **17**(12), 1063–1072 (2008)
 18. E. Sparr et al., "Controlling the hydration of the skin through the application of occluding barrier creams," *J. R. Soc. Interface* **10**(80), 20120788 (2012).
 19. B. Li, P. Borri, and W. Langbein, "Dual/differential coherent anti-Stokes Raman scattering module for multiphoton microscopes with a femtosecond Ti:sapphire oscillator," *J. Biomed. Opt.* **18**(6), 066004 (2013).
 20. K. König et al., "Optical skin biopsies by clinical CARS and multiphoton fluorescence/SHG tomography," *Laser Phys. Lett.* **8**(6), 465–468 (2011).
 21. H. Kano and H. O. Hamaguchi, "Vibrationally resonant imaging of a single living cell by supercontinuum-based multiplex coherent anti-Stokes Raman scattering microspectroscopy," *Opt. Express* **13**(4), 1322–1327 (2005).
 22. D. Li et al., "In vivo and simultaneous multimodal imaging: Integrated multiplex coherent anti-Stokes Raman scattering and two-photon microscopy," *Appl. Phys. Lett.* **97**(22), 223702 (2010).
 23. A. D. Slepikov et al., "Multimodal CARS microscopy of structured carbohydrate biopolymers," *Biomed. Opt. Express* **1**(5), 1347–1357 (2010).
 24. M. Balu et al., "In Vivo multiphoton NADH fluorescence reveals depth-dependent keratinocyte metabolism in human skin," *Biophys. J.* **104**(1), 258–267 (2013).
 25. K. Miyamoto and H. Kudoh, "Quantification and visualization of cellular NAD(P)H in young and aged female facial skin with *in vivo* two-photon tomography," *Br. J. Dermatol.* **169**S2, 25–31 (2013).
 26. M. Balu et al., "Clinical studies of pigmented lesions in human skin by using a multiphoton tomograph," *Proc. SPIE* **8588**, 858812 (2013).
 27. A. Uchugonova et al., "Watching stem cells in the skin of living mice noninvasively," *Cell Cycle* **10**(12), 2017–2020 (2011).
 28. M. Balu et al., "Distinguishing between benign and malignant melanocytic nevi by *in vivo* multiphoton microscopy," *Cancer Res.* **74**(10), 2688–2697 (2014).
 29. E. Dimitrow et al., "Sensitivity and specificity of multiphoton laser tomography for *in vivo* and *ex vivo* diagnosis of malignant melanoma," *J. Investig. Dermatol.* **129**(7), 1752–1760 (2009).
 30. M. J. Koehler et al., "In vivo assessment of human skin aging by multiphoton laser scanning tomography," *Opt. Lett.* **31**(19), 2879–2881 (2006).
 31. S. Hell and E. H. K. Stelzer, "Properties of a 4Pi confocal fluorescence microscope," *J. Opt. Soc. Am. A* **9**(12), 2159–2166 (1992).
 32. W. S. Rasband, "ImageJ," U. S. National Institutes of Health, Bethesda, USA (1997–2014).
 33. T. Hellerer, A. M. K. Enejder, and A. Zumbusch, "Spectral focusing: High spectral resolution spectroscopy with broad-bandwidth laser pulses," *Appl. Phys. Lett.* **85**(1), 25–27 (2004).
 34. H. Kano, "Molecular spectroscopic imaging using a white-light laser source," *Bull. Chem. Soc. Japan* **83**(7), 735–743 (2010).
 35. V. Ulrich et al., "Compact multiphoton/single photon laser scanning microscope for spectral imaging and fluorescence lifetime imaging," *Scanning* **26**(5), 217–225 (2004).
 36. R. Sjöback, J. Nygren, and M. Kubista, "Absorption and fluorescence properties of fluorescein," *Spectrochim. Acta Pt A* **51**, 7–21 (1995).
 37. A. Bailey and K. Rollefson, "The determination of the fluorescence lifetimes of dissolved substances by a phase shift method," *J. Chem. Phys.* **21**, 1315–1322 (1953).
 38. P. J. Caspers, G. W. Lucassen, and G. J. Puppels, "Combined *in vivo* confocal Raman spectroscopy and confocal microscopy of human skin," *Biophys. J.* **85**(1), 572–580 (2003).
 39. C. L. Evans and X. S. Xie, "Coherent anti-stokes Raman scattering microscopy: chemical imaging for biology and medicine," *Annu. Rev. Anal. Chem.* **1**, 883–909 (2008).
 40. P. J. Caspers et al., "In vivo confocal Raman microspectroscopy of the skin: noninvasive determination of molecular concentration profiles," *J. Investig. Dermatol.* **116**(3), 434–442 (2001).
 41. H. Chen et al., "A multimodal platform for nonlinear optical microscopy and microspectroscopy," *Opt. Express* **17**(3), 1282–90 (2009).
 42. H. C. Gerritsen et al., "Fluorescence lifetime imaging in scanning microscopy," in *Handbook of Biological Confocal Microscopy*, J. Pawley, Ed., pp. 516–532, Springer, New York (2006).
 43. A. Masood and A. Ali Al-Jumaily, "Computer aided diagnostic support system for skin cancer: a review of techniques and algorithms," *Int. J. Biomed. Imaging* **2013**, 1–22 (2013).
 44. S. R. Kandelhardt et al., "Imaging of brain and brain tumor specimens by time-resolved multiphoton excitation microscopy *ex vivo*," *Neuro-Oncology* **9**(2), 103–112 (2007).

Martin Weinigel graduated in biomedical engineering at the University of Applied Sciences Jena in 2007. He wrote his diploma thesis at the Department of Screening and Rare Cell Detection Technologies at The Burnham Institute for Medical Research, San Diego, USA. In 2010, he received an ME degree in laser- and optotechnology of the University of Applied Sciences in Jena. His current research includes the development of multimodal imaging systems at the JenLab GmbH, Germany.

Hans Georg Breunig is a research scientist at JenLab GmbH and Saarland University, Germany. He holds a master's degree in physics from the University of Maryland at College Park, USA, and received a PhD in physics from the University of Bremen, Germany, in 2003. He has worked for more than 10 years on applications of femtosecond lasers in different research fields and is the author of more than 30 journal papers.

Aisada Uchugonova received her master's degree in biomedical sciences from the National University of Kyrgyzstan and her PhD degree from the Saarland University, Germany, in 2009. She served as a postdoctoral researcher at the University of California, San Diego. She is currently PI on the DFG funded project in the Department of Biophotonics and Laser Technology, Saarland University. Her research interests include noninvasive and label-free imaging, optical characterization of stem cells, and nanosurgery of cells.

Karsten König is full professor and head of the Department of Biophotonics and Laser Technologies at the Saarland University. He is president of the company JenLab GmbH. He gained the PhD degree in physics and habilitation degree in cell biology from the University Jena. He published about 500 scientific papers in the field of biophotonics and laser material processing and pioneered fluorescence lifetime imaging, femtosecond laser nanoprocessing, laser transfection, and clinical multiphoton tomography.